Inorg. Chem. **2008**, *47*, 4762−4773

On the Origin of Circular Dichroism in Trigonal Dihedral Cobalt (III) Complexes of Unsaturated Bidentate Ligands

Jing Fan and Tom Ziegler*

Department of Chemistry, University of Calgary, 2500 University Drive, Calgary, Alberta, Canada, T2N 1N4

Received January 14, 2008

The circular dichroism spectra of the complexes $Co(acac)_3$, $[Co(ox)_3]^{3-}$, $[Co(mal)_3]^{3-}$, and $[Co(Thiox)_3]^{3-}$ with acac = acetylacetonate, ox = oxalate, mal = malonate, Thiox = dithioxalate, have been investigated computationally employing time-dependent density functional theory. A detailed comparison of the experimental and theoretical results is made. Rotatory strengths associated with typical electronic transitions in the complexes containing unsaturated ligands are interpreted within a qualitative framework in terms of transition moments for excitations within a single ligand.

1. Introduction

Circular dichroism (CD) spectroscopy[1,2] of transition metal complexes has been used for a long time as a tool to deduce the stereochemistry of chiral metal complexes. Early theoretical approaches to the chiroptical properties of transition metal compounds include methods based on crystal field theory,[3] molecular orbital theory[4,5] and subsequent theoretical developments.[6,7] They have focused almost exclusively on the interpretation of CD from d-to-d transitions in complexes with saturated diamine ligands. However $\pi \rightarrow \pi^*$ internal ligand transitions have also been considered.[8−10]

Compounds containing unsaturated ligands, typically oxalate and acetylacetonate, have a somewhat more complicated electronic structure than the amine systems as there are in addition to the σ-based ligand orbitals also participations from π-type ligand orbitals to the electronic structure. Excitations involving the π-orbitals on the ligands introduce additional challenges in the assignment and interpretation of the CD spectra.

Time-dependent density functional theory (TD-DFT), which provides reliable accuracy with low computational cost, has become an important method for the study of optical activity.[11,12] Recent studies[13−15] of chiral complexes show fair agreement between TD-DFT and experimental CD spectra. Preliminary results on the CD of $Co(acac)_3$ and $[Co(ox)_3]^{3-}$ have been reported in previous papers.[14,15] No detailed interpretation concerning the origin of the optical activity in these complexes has been given.

In the present work the TD-DFT method is applied to evaluate the CD spectra of Co^{III} complexes Λ-$Co(acac)_3$, Λ-$[Co(ox)_3]^{3-}$, Δ-$[Co(mal)_3]^{3-}$, and Δ-$[Co(Thiox)_3]^{3-}$ (acac = acetylacetonate, ox = oxalate, mal = malonate, Thiox = dithioxalate, Scheme 1). A qualitative framework is proposed to analyze the CD spectra of coordination compounds with bidentate ligands containing both σ- and π-orbitals.

* To whom correspondence should be addressed. E-mail: ziegler@ucalgary.ca.

(1) Cotton, A. *C. R. Hebd. Seances Acad. Sci.* **1895**, *120*, 989–1044.
(2) *Circular Dichroism: Principle and Applications*; 2nd ed.; Berova, N., Nakanishi, K., Woody, R. W., Eds.; Wiley-VCH: New York, 2000.
(3) Moffitt, W. *J. Chem. Phys.* **1956**, *25*, 1189–1198.
(4) Liehr, A. D. *J. Phys. Chem.* **1964**, *68*, 665–722.
(5) Karipides, A.; Piper, T. S. *J. Chem. Phys.* **1964**, *40*, 674–682.
(6) Stickland, R. W.; Richardson, F. S. *Inorg. Chem.* **1973**, *12*, 1025–1036.
(7) Evans, R. S.; Schreiner, A. F.; Hauser, P. J. *Inorg. Chem.* **1974**, *13*, 2185–2192.
(8) Mason, S. F. *Pure Appl. Chem.* **1970**, *24*, 335.
(9) Bosnich, B. *Acc. Chem. Res.* **1966**, *2*, 266.
(10) Guennic, B. L.; Hieringer, W.; Görling, A.; Autschbach, J. *J. Phys. Chem. A* **2005**, *109*, 4836–4846.
(11) Casida, M. E. Time-dependent density functional response theory for molecules. In *Recent advances in density functional methods*; Chong, D. P., Ed.; World Scientific: Singapore, 1995; Vol. *1*.
(12) Dobson, J. F. Time-denpendent density functional theory. In *Electronic density functional theory. Recent progress and new directions*; Dobson, J. F., Vignale, G., Das, M. P., Eds.; Plenum Press: New York, 1998.
(13) Jorge, F. E.; Autschbach, J.; Ziegler, T. *J. Am. Chem. Soc.* **2005**, *127*, 975–985.
(14) Jorge, F. E.; Autschbach, J.; Ziegler, T. *Inorg. Chem.* **2003**, *42*, 8902–8910.
(15) Autschbach, J.; Jorge, F. E.; Ziegler, T. *Inorg. Chem.* **2003**, *42*, 2867–2877.

10.1021/ic800072k CCC: $40.75
Published on Web 04/25/2008

Scheme 1. Structure of Ligands Studied

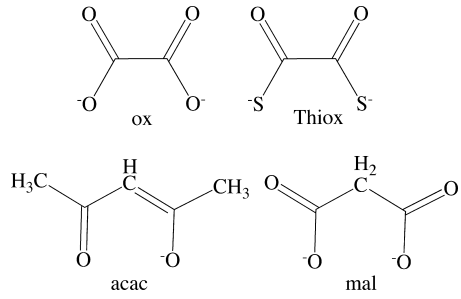

2. Computational Details

The computations reported here have been carried out with a modified version of the Amsterdam Density Functional (ADF) program package.[10,16–18] The CD version by Autschbach et al.[19–21] is an extension of the TD-DFT module in ADF developed by van Gisbergen, Baerends, et al.[22–24] The valence triple-ζ polarized "TZP" Slater basis sets from the ADF database were employed in all calculations. The ls^2 shells on C and O and the $ls^2 2s^2 2p^6$ shells on S and Co were considered frozen. Rotatory strengths were calculated by the dipole-length formula. It has been shown[15] for $[Co(en)_3]^{3+}$ that rotatory strengths computed with this formula are in good agreement with those obtained from the dipole-velocity form. Typically, the 40 lowest excitations were calculated (in some cases 50). On the basis of the computed singlet excitation energies, associated oscillator strengths and rotatory strengths, CD spectra have been simulated and compared with experimental data. A reasonable overall agreement with experiment was obtained by choosing a Gaussian half-width parameter σ of 0.13 eV for all simulated spectra except for $[Co(Thiox)_3]^{3-}$, for which the empirical recipe[25] has been employed to simulate the spectrum with the bandwidth $\Delta\bar{\nu}$ given by $\Delta\bar{\nu} = 7.5\sqrt{\bar{\nu}}$, where $\bar{\nu}$ is the absorption frequency in cm^{-1}. Numerical data for the experimental spectra have been extracted using the "g3data" software.[26]

The Vosko−Wilk−Nusair (VWN)[27] local density approximation (LDA) with the Becke88-Perdew86 (BP86) gradient corrections[28,29] have been used in the CD calculations. All TD-DFT calculations have been carried out based on optimized geometries (VWN functional, TZP basis set). The "COnductor-like continuum Solvent MOdel" (COSMO)[30,31] has been applied in the calculations of the CD spectra to simulate the solvent effect on the complex ions.

Scheme 2. Configurations of $[M(L\text{-}L)_3]^{n+}$.

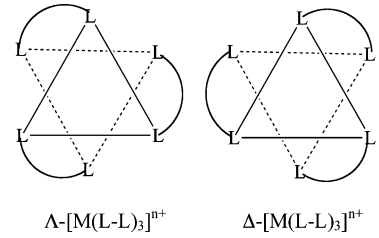

3. Results and Discussion

3.1. Geometrical Parameters for the $[M(L\text{-}L)_3]^{n+}$ Complexes. The two possible enantiomeric configurations of the title complexes are shown in Scheme 2. The molecules have D_3 symmetry, and the essentially planar ligands have C_{2v} symmetry. It is noted that the methylene carbon atom on the malonate ligand may distort from the main plane.[32] However, such a distortion is not considered in the present work.

To understand the factors that contribute to the CD spectra of the title complexes, we start with a hypothetical configuration of the molecules, see Figure 1a. The configuration has D_{3h} symmetry and the planes of the three ligands, denoted by rectangles, are situated parallel to the C_3 axis, along the z-direction of the figure. No optical activity is present in this configuration because of its symmetry.

As we can see from Figure 1b, a counterclockwise rotation (from the point of view of an observer looking along the axis of rotation toward the metal) of the three ligand planes by ω degrees leads to the Λ-configuration of $[M(L\text{-}L)_3]^{n+}$, which has D_3 symmetry and thus in principle can exhibit optical activity. Obviously, a rotation by $-\omega$ would have resulted in the Δ-configuration of the complexes.

Whereas the polar ratio (s/h) and azimuthal angle (ϕ) are used traditionally[33] as a measure of the chiral distortion of the six ligating atoms away from the ideal octahedrons, the rotation angle ω introduced here can be used alternatively to discuss chirality, see Figure 2. The two sets of parameters are related by:

$$s/h = \sqrt{3(b^2 + a^2 \sin^2 \omega)}/(2a \cos \omega) \quad (1)$$

$$\phi = 2 \arctan[(a \sin \omega)/b] \quad (2)$$

Here a is the half-distance between the two ligating atoms on the ligand, and b is the distance between the metal and the midpoint of the same two atoms, see Figure 2a. We recall

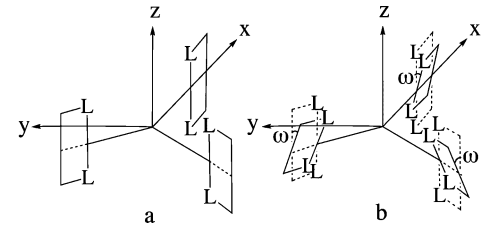

Figure 1. (a) Structure of $[M(L\text{-}L)_3]^{n+}$ with D_{3h} symmetry, (b) structure of Λ-$[M(L\text{-}L)_3]^{n+}$ with D_3 symmetry after a rotation of the ligand ring planes by ω degrees.

(16) Fonseca Guerra, C.; Visser, O.; Snijders, J. G.; te Velde, G.; Baerends, E. J. Parallelisation of the Amsterdam Density Functional Program. In *Methods and Techniques for Computational Chemistry*; STEF: Cagliari, 1995.
(17) te Velde, G.; Bickelhaupt, F. M.; Baerends, E. J.; van Gisbergen, S. J. A.; Fonseca Guerra, C.; Snijders, J. G.; Ziegler, T. *J. Comput. Chem.* **2001**, *22*, 931–967.
(18) *Amsterdam Density Functional program*; Theoretical Chemistry, Vrije Universiteit: Amsterdam; 2008 URL: http://www.scm.com.
(19) Autschbach, J.; Ziegler, T.; van Gisbergen, S. J. A.; Baerends, E. J. *J. Chem. Phys.* **2002**, *116*, 6930–6940.
(20) Autschbach, J.; Ziegler, T. *J. Chem. Phys.* **2002**, *116*, 891–896.
(21) Autschbach, J.; Ziegler, T.; Patchkovskii, S.; van Gisbergen, S. J. A.; Baerends, E. J. *J. Chem. Phys.* **2002**, *117*, 581–592.
(22) van Gisbergen, S. J. A.; Snijders, J. G.; Baerends, E. J. *J. Chem. Phys.* **1995**, *103*, 9347–9354.
(23) van Gisbergen, S. J. A.; Snijders, J. G.; Baerends, E. *J. Comput. Phys. Commun.* **1999**, *118*, 119–138.
(24) van Gisbergen, S. J. A.; Fonseca-Guerra, C.; Baerends, E. J. *J. Comput. Chem.* **2000**, *21*, 1511–1523.
(25) Brown, A.; Kemp, C. M.; Mason, S. F. *J. Chem. Soc. A* **1971**, 751–755.
(26) Frantz, J. "g3data", 2008 URL: http://www.frantz.fi/software/g3data.php.
(27) Vosko, S. H.; Wilk, L.; Nusair, M. *Can. J. Phys.* **1980**, *58*, 1200–1211.
(28) Becke, A. D. *Phys. Rev. A* **1988**, *38*, 3098–3100.
(29) Perdew, J. P. *Phys. Rev. B* **1986**, *33*, 8822–8824.

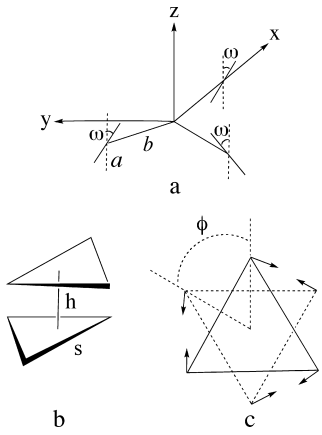

Figure 2. (a) Geometry parameters in $[M(L\text{-}L)_3]^{n+}$, (b) polar ratio in hexacoordinate complexes with O_h geometry corresponding to $s/h = 1.22$, (c) azimuthal angle in hexacoordinate complexes with O_h geometry corresponding to $\phi = 60°$.

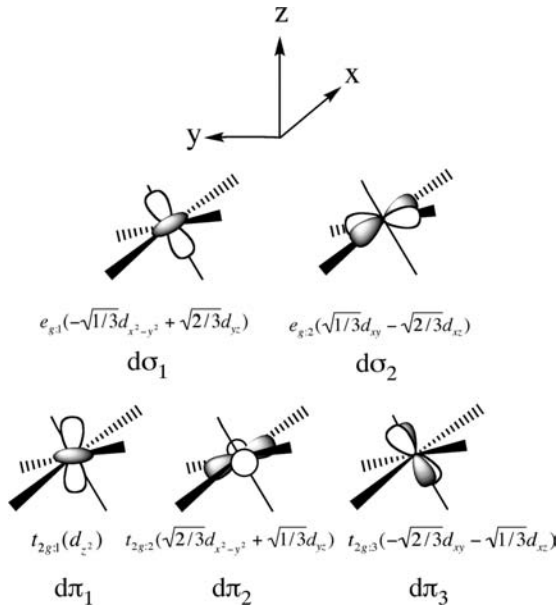

Figure 3. Metal *n*d orbitals in octahedral representation.

that for an ideal octahedron, $s/h = 1.22$ and $\phi = 60°$, which corresponds to $a = b$ and $\omega = 35.3°$. The rotation angles obtained from geometry optimizations are 36.4°, 35.1°, 36.5°, and 32.1° for $Co(acac)_3$, $[Co(ox)_3]^{3-}$, $[Co(mal)_3]^{3-}$, and $[Co(Thiox)_3]^{3-}$, respectively.

3.2. Metal−Ligand Orbital Interaction. Of importance for the complex formation are the *n*d orbitals on the metal center as well as the ligand-based σ- and π-type orbitals. The *n*d orbitals on the metal ions are $d\pi_1$, $d\pi_2$, and $d\pi_3$ of t_{2g} symmetry in the O_h parentage. These orbitals transform as a_1 and e in D_3 symmetry, respectively, see Figure 3. There are in addition the $d\sigma_1$ and $d\sigma_2$ metal orbitals of e_g symmetry in the O_h parentage transforming as e in D_3 symmetry.

The ligand-based lone-pair σ-orbitals on a ligand ring are shown in Figure 4, where they are labeled "a_1" and "b_2" according to C_{2v} symmetry. The linear combinations of equivalent orbitals on different rings making up the symmetry ligand σ-orbitals in $[M(L\text{-}L)_3]^{n+}$ according to D_3 (or D_{3h}) symmetry are listed in Table 1 where the ligand MOs of a_1 symmetry are denoted as $\alpha_i^\sigma$and those of b_2 symmetry as β_i^σ

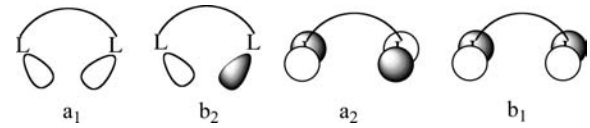

Figure 4. Ligand σ- and π-orbitals on coordinated atoms.

Table 1. Symmetry Ligand Orbitals in $[M(L\text{-}L)_3]^{n+}$ of D_3 Symmetry.

symmetry π-orbitals[a]		symmetry σ-orbitals[b]	
a_1^π	$(1/\sqrt{3})(\alpha_1^\pi + \alpha_2^\pi + \alpha_3^\pi)$	a_1^σ	$(1/\sqrt{3})(\alpha_1^\sigma + \alpha_2^\sigma + \alpha_3^\sigma)$
a_2^π	$(1/\sqrt{3})(\beta_1^\pi + \beta_2^\pi + \beta_3^\pi)$	a_2^σ	$(1/\sqrt{3})(\beta_1^\sigma + \beta_2^\sigma + \beta_3^\sigma)$
$1e_x^\pi$	$(1/\sqrt{6})(-2\alpha_1^\pi + \alpha_2^\pi + \alpha_3^\pi)$	$1e_x^\sigma$	$(1/\sqrt{6})(-2\alpha_1^\sigma + \alpha_2^\sigma + \alpha_3^\sigma)$
$1e_y^\pi$	$(1/\sqrt{2})(-\alpha_2^\pi + \alpha_3^\pi)$	$1e_y^\sigma$	$(1/\sqrt{2})(-\alpha_2^\sigma + \alpha_3^\sigma)$
$2e_x^\pi$	$(1/\sqrt{2})(-\beta_2^\pi + \beta_3^\pi)$	$2e_x^\sigma$	$(1/\sqrt{2})(-\beta_2^\sigma + \beta_3^\sigma)$
$2e_y^\pi$	$(1/\sqrt{6})(2\beta_1^\pi - \beta_2^\pi - \beta_3^\pi)$	$2e_y^\sigma$	$(1/\sqrt{6})(2\beta_1^\sigma - \beta_2^\sigma - \beta_3^\sigma)$

[a] α_i^π is a ligand π-orbital on ring $i(1,3)$ of a_2 symmetry; β_i^π is ligand π-orbital on ring $i(1,3)$ of b_1 symmetry. [b] α_i^σ is a ligand σ-orbital on ring i (1,3) of a_1 symmetry; β_i^σ is a ligand σ-orbital on ring i (1,3) of b_2 symmetry.

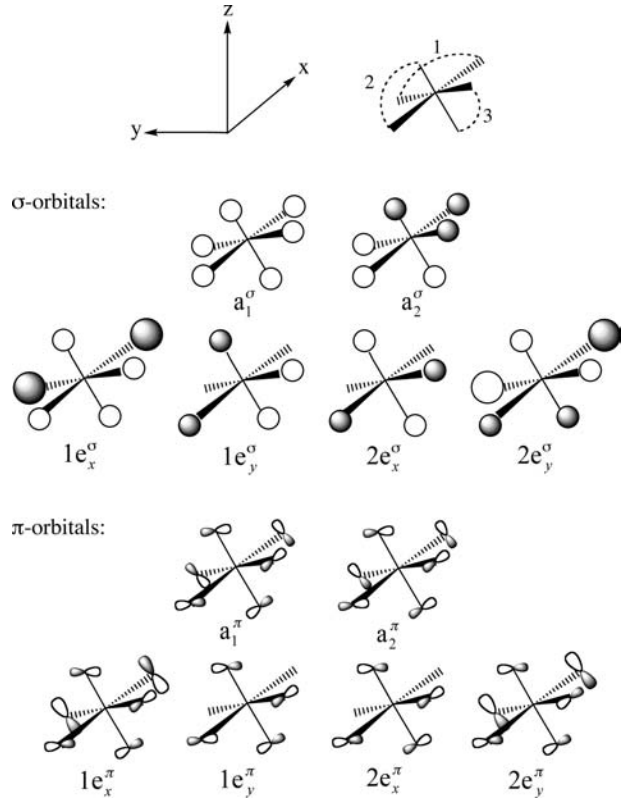

Figure 5. Symmetry ligand σ- and π-orbitals of $[M(L\text{-}L)_3]^{n+}$ with numbering of the three ligands.

with the subscript indicating the ring they belong to. The same symmetry combinations are displayed schematically in Figure 5. On the other hand, the unsaturated ligands contain in addition π-orbitals that are perpendicular to the ligand ring planes. The π-orbitals on the two ligating donor atoms are also shown in Figure 4, where the resulting ligand MOs are labeled "a_2" and "b_1" according to C_{2v} symmetry. For full consideration, all the π-orbitals on a ligand should be included to give the "a_2" and "b_1" orbitals, as they are in our numerical calculations. However, in our qualitative overlap considerations, only the π-orbitals situated on the ligating atoms are considered as they play the major role in the metal−ligand orbital interactions. Similar to the σ-orbitals, linear combinations of the equivalent π MOs on different

Table 2. Unique Overlaps between the Metal *n*d Orbitals[a] and the Symmetry Ligand Orbitals[b] of $[M(L\text{-}L)_3]^{n+}$ with D_3 Symmetry[c,d,e]

σ-overlap	expression	π-overlap	expression
$S(d\sigma_1,1e_x^{\sigma});S(d\sigma_2,1e_y^{\sigma})$	$[b/(2a)][(1/\sqrt{2})(b^2 - a^2\sin^2\omega)/b^2] + (a^2\sin 2\omega)/b^2]S_{xz}{}^0$	$S(d\sigma_1,1e_x^{\pi});S(d\sigma_2,1e_y^{\pi})$	$\cos\theta\,[(1/\sqrt{2})\sin 2\omega - 2\cos 2\omega]S_\pi$
$S(d\sigma_1,2e_x^{\sigma});S(d\sigma_2,2e_y^{\sigma})$	$[(1/\sqrt{2})\sin\omega + \cos\omega]S_{xz}{}^0$	$S(d\sigma_1,2e_x^{\pi});S(d\sigma_2,2e_y^{\pi})$	$\sin\theta\,(\sqrt{2}\cos\omega - 2\sin\omega)S_\pi$
$S(d\pi_1,a_1^{\sigma})$	$-[(3\sqrt{3})/2][(a^2\cos^2\omega)/(a^2 + b^2) - (1/3)]S_\sigma$	$S(d\pi_1,a_1^{\pi})$	$3(\cos\theta\sin 2\omega)S_\pi$
$S(d\pi_2,1e_x^{\sigma});S(d\pi_3,1e_y^{\sigma})$	$-[b/(2a)][(b^2 - a^2\sin^2\omega)/b^2) - (1/\sqrt{2})(a^2\sin 2\omega)/b^2)]S_{xz}{}^0$	$S(d\pi_2,1e_x^{\pi});S(d\pi_3,1e_y^{\pi})$	$-\cos\theta\,(\sin 2\omega + \sqrt{2}\cos 2\omega)S_\pi$
$S(d\pi_2,2e_x^{\sigma});S(d\pi_3,2e_y^{\sigma})$	$-[\sin\omega - (1/\sqrt{2})\cos\omega]S_{xz}{}^0$	$S(d\pi_2,2e_x^{\pi});S(d\pi_3,2e_y^{\pi})$	$-\sin\theta\,(2\cos\omega + \sqrt{2}\sin\omega)S_\pi$

[a] See Figure 3. [b] See Table 1 and Figure 5. [c] $S_{xz}{}^0 = [(\sqrt{3ab}/(a^2 + b^2)]S_\sigma$, $\sin\theta = [(a^2\sin^2\omega + b^2)/(a^2 + b^2)]^{1/2}$, and $\cos\theta = (a\cos\omega)/\sqrt{a^2+b^2}$. [d] S_σ is the overlap between a d_{z^2} orbital on the metal and a σ-ligand orbital pointing along the *z*-axis toward the metal. [e] S_π is the overlap between a d_{xz} orbital on the metal and a $2p_z$ orbital situated on an atom at a distance *R* from the metal center along the *x*-axis.

Table 3. Calculated Unique Overlaps between the Metal *n*d Orbitals and the Symmetry Ligand Orbitals[a]

overlaps	case I[b]	case II[c]
	σ-Type	
$S(d\sigma_1,1e_x^{\sigma});S(d\sigma_2,1e_y^{\sigma})$	$0.612S_\sigma$	$0.610S_\sigma$
$S(d\sigma_1,2e_x^{\sigma});S(d\sigma_2,2e_y^{\sigma})$	$1.061S_\sigma$	$1.058S_\sigma$
$S(d\pi_1,a_1^{\sigma})$	0	$-0.034S_\sigma$
$S(d\pi_2,1e_x^{\sigma});S(d\pi_3,1e_y^{\sigma})$	0	$-0.064S_\sigma$
$S(d\pi_2,2e_x^{\sigma});S(d\pi_3,2e_y^{\sigma})$	0	$0.059S_\sigma$
	π-Type	
$S(d\sigma_1,1e_x^{\pi});S(d\sigma_2,1e_y^{\pi})$	0	$-0.138S_\pi$
$S(d\sigma_1,2e_x^{\pi});S(d\sigma_2,2e_y^{\pi})$	0	$0.110S_\pi$
$S(d\pi_1,a_1^{\pi})$	$1.632S_\pi$	$1.590S_\pi$
$S(d\pi_2,1e_x^{\pi});S(d\pi_3,1e_y^{\pi})$	$-0.816S_\pi$	$-0.892S_\pi$
$S(d\pi_2,2e_x^{\pi});S(d\pi_3,2e_y^{\pi})$	$-2.002S_\pi$	$-1.976S_\pi$

[a] See Table 2 for the definition of overlaps. [b] Octahedron case with $a = b$, $\omega = 35.3°$. [c] Real geometry of $[Co(Thiox)_3]^{3-}$, $a = 1.542$, $b = 1.596$, and $\omega = 32.1°$.

rings make up the symmetry ligand orbitals in $[M(L\text{-}L)_3]^{n+}$ according to D_3 (or D_{3h}) symmetry. These combinations are listed in Table 1 where the ligand MOs of a_2 symmetry are denoted as α_i^{π} and those of b_1 symmetry as β_i^{π} with the subscript indicating the ring they belong to. The symmetry ligand π-orbitals are also displayed in Figure 5. Unlike the universal σ-orbitals on the ligating atoms, the π MOs involved vary in shapes and numbers from one ligand to another. We might on occasion write the symmetry ligand π-orbitals in Table 1 as $a_1^{\pi}(na_2)$, $a_2^{\pi}(nb_1)$, $1e_x^{\pi}(na_2)$, $1e_y^{\pi}(na_2)$, $2e_x^{\pi}(nb_1)$, and $2e_y^{\pi}(nb_1)$, with *n* indicating from which ligand MOs the symmetry combination was constructed.

To analyze the bonding in $[M(L\text{-}L)_3]^{n+}$, we have derived expressions for the overlaps between the metal d-orbitals and the symmetry ligand orbitals. The symmetry unique overlaps are expressed in terms of the geometry parameters of the complexes for both σ- and π-interactions, see Table 2. We note again that in deriving the overlaps involving ligand π-orbitals, only the AOs on the ligating atoms are taken into account. In the ideal octahedral case, there is $a = b$ and $\omega = 35.3°$, and the corresponding overlaps involving both σ- and π-orbitals are listed as Case I in Table 3. It is apparent that in a perfect octahedral arrangement of the six ligating atoms, the metal d-orbitals $d\pi_1$, $d\pi_2$, and $d\pi_3$ will only overlap with the symmetry ligand π-orbitals, whereas $d\sigma_1$ and $d\sigma_2$ will only overlap with the σ-orbitals. When the six coordinated atoms are distorted from the ideal octahedron, the same metal d-orbital might interact with both π- and σ-orbitals on the ligand. In Case II of Table 3, $[Co(Thiox)_3]^{3-}$ of D_3 symmetry is taken as an example for which calculations of the overlaps between the metal d-orbitals and the symmetry ligand orbitals are carried out with the parameters $a = 1.542$, $b = 1.596$, and $\omega = 32.1°$ obtained from geometry optimizations. It is readily seen that with the distorted octahedral geometry, the orbitals $d\pi_1$, $d\pi_2$, and $d\pi_3$ that originally overlap only with ligand π-orbitals now in addition overlap slightly with the σ-orbitals. Likewise, the $d\sigma_1$ and $d\sigma_2$ orbitals now in addition overlap with the ligand π-orbitals.

The group overlaps now allow us to construct a simplified orbital interaction diagram for $[M(L\text{-}L)_3]^{n+}$. The left side of Figure 6 considers only the σ-interaction between the metal $d\sigma$ orbitals and the symmetry ligand σ-orbitals. We have one strongly ligand-based bonding MO $1\tilde{e}^{\sigma}$ followed by a set of nonbonding orbitals $2\tilde{e}^{\sigma}$, $1\tilde{a}_1^{q}$, and $1\tilde{a}_2^{q}$ and a strongly antibonding $d\sigma$-based orbital $3\tilde{e}(d\sigma)$. In O_h symmetry, $1\tilde{e}^{\sigma}$ and $3\tilde{e}^{\sigma}$ would have made up the e_g bonding and e_g antibonding combinations whereas $1\tilde{a}_1^{q}$, $(2\tilde{e}^{\sigma},1\tilde{a}_2^{q})$ would have constituted the a_{1g} and t_{1u} ligand-based MOs.[34]

On the other hand, the expressions for the π-group overlaps allow us to construct a qualitative π-interaction diagram as shown to the right in Figure 6. At lowest energy we have the bonding MOs $1\tilde{e}^{\pi}$, $2\tilde{e}^{\pi}$, and $1\tilde{a}_1^{q}$ as linear combinations of ligand and $d\pi$ components transforming as, respectively, a_1 and e symmetry under the D_3 environment. Above are the nonbonding $1\tilde{a}_2^{q}$ ligand-based levels. The $3\tilde{e}^{\pi}$ and $2\tilde{a}_1^{q}$ orbitals are antibonding with respect to $d\pi$ and the symmetry ligand combinations made up of occupied nb_1 and na_2 ring orbitals. The $3\tilde{e}^{\pi}$ and $2\tilde{a}_1^{q}$ orbitals can however be stabilized by interactions with ligand symmetry orbitals made up of virtual mb_1 and ma_2 ligand combinations. We have further at highest energy $2\tilde{a}_2^{q}$, $4\tilde{e}^{\pi}$, $5\tilde{e}^{\pi}$, and $3\tilde{a}_1^{q}$ made up of mb_1 and ma_2 ligand orbitals.

We can finally obtain a rough picture of the electronic structure in $[M(L\text{-}L)_3]^{n+}$ by combining the σ- and π-levels in Figure 6. It is important to point out that in constructing the MO diagram, we neglect the interaction between the metal $d\sigma$ set and the ligand π-orbitals, as well as that between the $d\pi$ set and the ligand σ-orbitals, as they will not change the energy levels significantly. However, such a mixing might be important for the CD intensities and will be taken into account in our numerical calculations. Also, although the highest occupied molecular orbitals (HOMOs) in the com-

(30) Klamt, A.; Schüürmann, G. *J. Chem. Soc., Perkin Trans.* **2 1993**, 799–805.
(31) Pye, C. C.; Ziegler, T. *Theor. Chem. Acc.* **1999**, *101*, 396–408.
(32) Butler, K. R.; Snow, M. R. *J. Chem. Soc., Dalton Trans.* **1976**, 251–258.
(33) Stiefel, E. I.; Brown, G. F. *Inorg. Chem.* **1972**, *11*, 434–436.
(34) Fan, J.; Ziegler, T. *Chirality*, accepted for publication.
(35) Von Dreele, R. B.; Fay, R. C. *J. Am. Chem. Soc.* **1971**, 4936–4938.

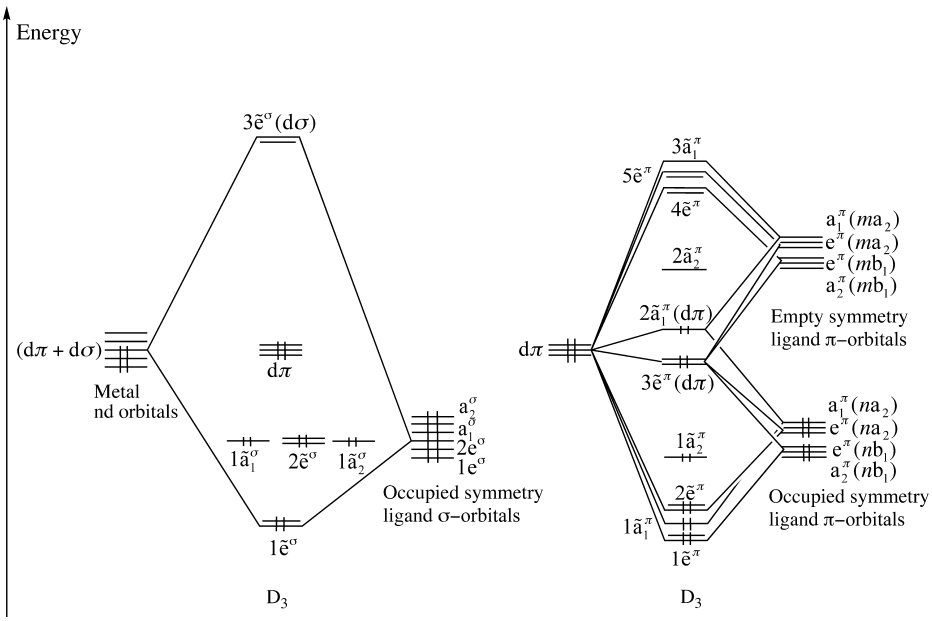

Figure 6. Metal−ligand orbital interaction diagram for $[M(L\text{-}L)_3]^{n+}$. Left side considers σ-interactions whereas right side considers π-interactions. The metal d-orbitals are given in Figure 4. The symmetry ligand orbitals are shown in Figure 5 and Table 1.

plexes are universally the metal-based t_{2g} orbitals, the lowest unoccupied molecular orbitals (LUMOs) are not necessarily the e_g* set. The position of destabilized ligand- and metal-based orbitals is shown here in an arbitrary order that might vary from system to system. We shall provide a more quantitative level diagram for each metal complex studied here as we discuss their individual CD spectra shortly.

3.3. Mechanism by Which Transitions Involving Ligand π/π^* Orbitals Contribute to the CD of Complexes Containing Unsaturated Ligands. In systems containing only saturated ligands such as $[Co(en)_3]^{3+}$, the CD spectrum is dominated by d-to-d and Lσ-to-d charge transfer transitions (L_σMCT).[13,34] These types of transitions will also be present in the title complexes containing unsaturated ligands. However, the mechanism by which d-to-d and Lσ-to-d charge transfer transitions contribute to the CD will not be repeated here as it has already been discussed previously.[34] In the complexes containing unsaturated ligands, we have in addition a number of transitions involving ligand-based π-orbitals. These transitions include internal $\sigma\rightarrow\pi^*$ and $\pi\rightarrow\pi^*$ excitations as well as dπ-to-Lπ^* (or Lπ-to-dσ) charge transfer ($ML_\pi CT$ or $L_\pi MCT$). We shall in the following discuss the mechanism by which these new transitions contribute to the CD of the title complexes.

The sign and magnitude of CD bands associated with the transition $0\rightarrow\lambda$ is determined by the rotatory strength $R_{0\lambda}$:

$$R_{0\lambda} = \mathrm{Im}\,\langle 0|\hat{\mathbf{\Theta}}|\lambda\rangle\cdot\langle\lambda|\hat{\mathbf{M}}|0\rangle \qquad (3)$$

where $\hat{\mathbf{\Theta}}$ and $\hat{\mathbf{M}}$ are the many-electron electronic and magnetic dipole moment operators.

We shall in section 3.4 present an extensive set of calculations on R according to eq 3 for all title complexes based on TD-DFT. A detailed analysis of the results reveals that not only the internal ligand transitions but also the $ML_\pi CT$ (or $L_\pi MCT$) excitations may have significant contributions to R from one-electron ligand-centered excitation integrals of the type $\langle L\pi|\hat{\boldsymbol{o}}|L\pi^*\rangle$, $\langle L\sigma|\hat{\boldsymbol{o}}|L\pi^*\rangle$, or $\langle L\sigma|\hat{\boldsymbol{o}}|L\sigma^*\rangle$, where $\hat{\boldsymbol{o}} = \hat{\boldsymbol{\mu}}$ or $\hat{\boldsymbol{m}}$, and $\hat{\boldsymbol{\mu}}$ is the one-electron electric dipole operator whereas $\hat{\boldsymbol{m}}$ is the corresponding magnetic dipole operator. We shall therefore examine the transition moments associated with the one-electron excitations localized on the ligands to understand the results presented in section 3.4 later.

Let us first consider the localized $\pi\rightarrow\pi^*$ one-electron ligand excitations. For such an excitation, the associated electric transition dipole moments are polarized in the plane of each individual ligand and may be directed either along the y'-axis (long axis) or the z'-axis (short axis) as shown in Scheme 3 where the prime is used to distinguish the local coordinate system on each individual ligand from the global coordinate system used for the metal complex. Along the long-axis, the excitations on a single ligand (C_{2v}) involve single ligand orbitals belonging to different representations, that is, $a_2\rightarrow b_1$, while in the case of a short-axis polarized transition, the orbitals involved on a single ligand are of the same representation, that is, $a_2\rightarrow a_2$ or $b_1\rightarrow b_1$. On the other hand, the magnetic dipole transition moments associated with one-electron excitations on a single ligand come from the $a_2\rightarrow b_1$ transition. They are polarized perpendicular to the molecular plane, along the x'-axis as shown in Scheme 3.

Consider next the $\sigma\rightarrow\pi^*$ excitations. Possible $\sigma\rightarrow\pi^*$ one-electron transition densities on a single ligand can have a_2 ($a_1\rightarrow a_2$ or $b_1\rightarrow b_2$) or b_1 ($a_1\rightarrow b_1$ or $b_2\rightarrow a_2$) symmetry. While the a_2 transition density gives rise to an electrically forbidden excitation, the b_1 symmetry generates an electric transition dipole moment along the x'-axis and an magnetic dipole moment in the y' direction, see Scheme 3.

Obviously, the transitions on an individual free ligand that involve perpendicular electric and magnetic transition dipole moments are optically inactive. In the complexes $[M(L\text{-}L)_3]^{n+}$ of the imaginary configuration with D_{3h} symmetry, such transitions are still optically inactive for polarizations along the three axis of the global coordinate system because the

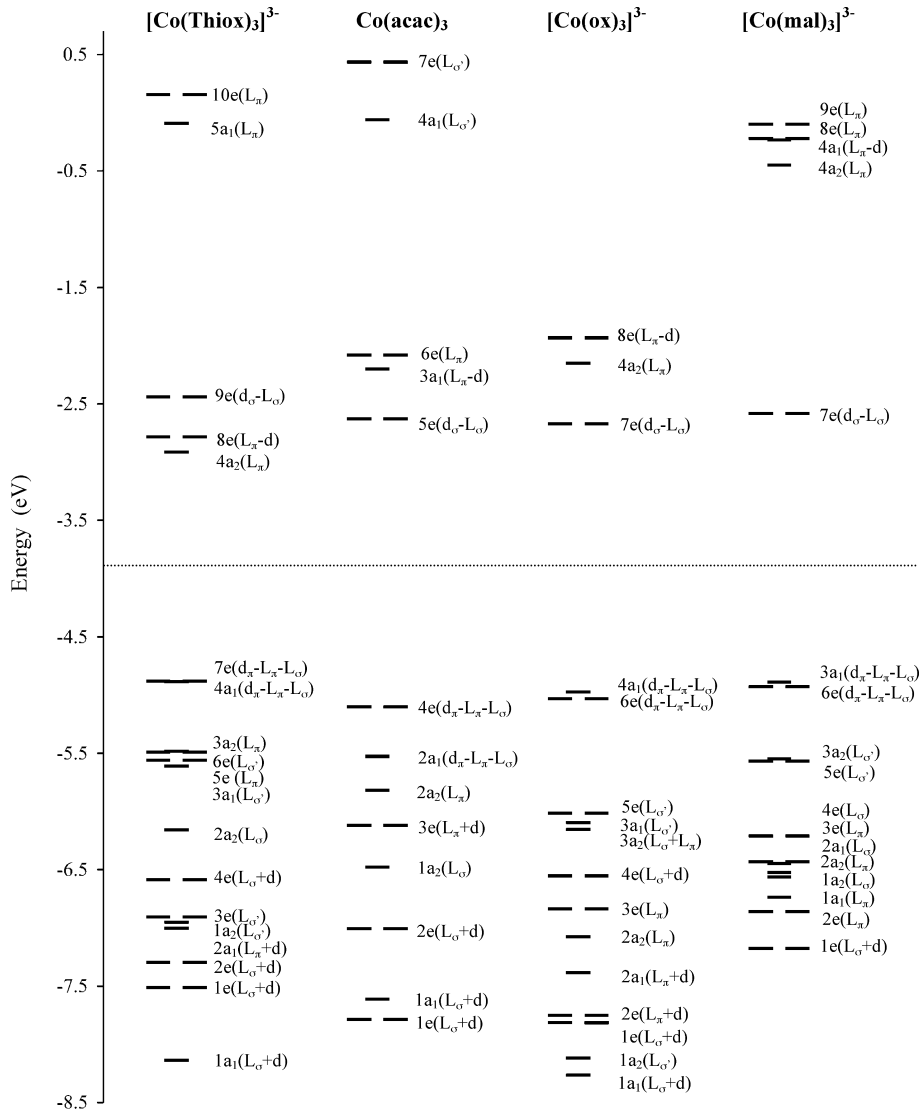

Figure 7. Molecular orbital diagrams from DFT calculations for the title complexes. The orbitals below the dotted line are occupied.

Scheme 3. Reference Axes in Thiox

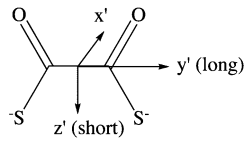

resultant product of the electric and magnetic transition dipole moments of each individual ligand is zero as can be seen from Figure 1a. When one or more of the ligands are rotated in the way described in Figure 1b, however, the reflection planes of the complex are removed which introduces chirality into the molecule and renders it optically active. In this case, the projection of the electric and magnetic transition dipole moments on each ligand onto the principal axis of the global coordinate system give rise to a nonzero rotatory strength. As a result one might be able to observe CD for light traveling along one of the global axis provided that this light is absorbed at a different frequency than light propagating along the other two directions. This will usually be the case because of the electric interaction between the ligands.

We shall now discuss the mechanism by which internal one-electron ligand transitions of the type $\sigma \rightarrow \pi^*$ and $\pi \rightarrow \pi^*$ can give rise to CD by contributing to R of eq 3. We start with contributions from $\pi \rightarrow \pi^*$ to R.

Consider a one-electron transition $k \rightarrow l$ involving two molecular orbitals k and l in a complex. Let further k have a contribution from a symmetry ligand orbital Lπ and l a contribution from a symmetry ligand orbital Lπ^*, Table 1. Let us further for the sake of argument and to give a concrete example assume that Lπ and Lπ^* are represented by symmetry ligand orbitals (D_3) of a_1 and a_2 designation, respectively. These symmetry orbitals are given as respectively a_1^{π} and a_2^{π} in Table 1.

We can now write the contribution from $a_1^{\pi} \rightarrow a_2^{\pi}$ to the rotatory strength of transition $k \rightarrow l$ as

$$R^{kl}(a_1^{\pi}, a_2^{\pi}) = c(k, a_1^{\pi})^2 c(l, a_2^{\pi})^2 \langle a_1^{\pi}|\hat{\boldsymbol{\mu}}|a_2^{\pi}\rangle \cdot \langle a_2^{\pi}|\hat{\boldsymbol{m}}|a_1^{\pi}\rangle$$
$$= [c(k, a_1^{\pi})^2 c(l, a_2^{\pi})^2/9]\langle(\alpha_1^{\pi} + \alpha_2^{\pi} + \alpha_3^{\pi})|\hat{\boldsymbol{\mu}}|\beta_1^{\pi} + \beta_2^{\pi} + \beta_3^{\pi}\rangle$$
$$\cdot \langle(\beta_1^{\pi} + \beta_2^{\pi} + \beta_3^{\pi})|\hat{\boldsymbol{m}}|(\alpha_1^{\pi} + \alpha_2^{\pi} + \alpha_3^{\pi})\rangle \quad (4)$$

Here α_i^{π} and β_i^{π} are single ligand π-orbitals as defined in

Table 1; $c(k,a_1^\pi)$ and $c(l,a_2^\pi)$ are the coefficients of a_1^π and a_2^π, respectively, in the two molecular orbitals given in general as

$$\psi_m = \sum_i^N c(m,i)\varphi_i \quad (5)$$

where $\{\varphi_i, i = 1, n\}$ is the set of symmetry ligand orbitals given in Table 1. In a detailed analysis one would have to identify α_i^π and β_i^π in terms of the ring orbitals $n\alpha_i^\pi$ and $n\beta_i^\pi$.

If we retain only integrals given by orbitals on the same ligands but neglect cross terms of the type $\langle\alpha_i^\pi|\hat{o}|\beta_j^\pi\rangle$ for $i \neq j$, then eq 4 reduces to

$$R^{kl}(a_1^\pi, a_2^\pi) = [c(k, a_1^\pi)^2 c(l, a_2^\pi)^2/9](\boldsymbol{\mu}_1 + \boldsymbol{\mu}_2 + \boldsymbol{\mu}_3)\cdot(\boldsymbol{m}_1 + \boldsymbol{m}_2 + \boldsymbol{m}_3) \quad (6)$$

where $\boldsymbol{\mu}_i = \langle\alpha_i^\pi|\hat{\boldsymbol{\mu}}|\beta_i^\pi\rangle$ and $\mathbf{m}_i = \langle\alpha_i^\pi|\hat{\mathbf{m}}|\beta_i^\pi\rangle$.

We note that the approximation in eq 6 is introduced here for the purpose of analysis. The numerical results reported later were calculated without such an approximation.

The contribution to $R_\gamma^{kl}(a_1^\pi,a_2^\pi)$ from $\boldsymbol{\mu}_i$ and $\mathbf{m}_i$ of each ligand with respect to light polarized along the γ-axis of the global coordinate system is the projection of $\boldsymbol{\mu}_i$ and $\mathbf{m}_i$ onto the γ-axis. We can readily express both $\boldsymbol{\mu}_i$ and $\mathbf{m}_i$ along the γ-direction in terms of the local ligand coordinate system of Scheme 3 and the ligand rotation ω. Further, $\boldsymbol{\mu}_i$, $(i = 1, 3)$ are all symmetry related and can be expressed in terms of $\boldsymbol{\mu}_1$ where the subscript refers to L_1 of Scheme 4. Likewise, $\boldsymbol{m}_i$, $(i = 1, 3)$ can all be expressed in terms of $\mathbf{m}_1$. We can then express in general $\langle L\pi|\hat{o}|L\pi^*\rangle$ integrals projected onto the global x-, y-, and z-axis in terms of ω and transition moments on L_1 with respect to the local coordinate system, see Table 4. From the knowledge of $\langle L\pi|\hat{o}|L\pi^*\rangle$ expressed in terms of $\boldsymbol{\mu}_1$ and $\mathbf{m}_1$ of Table 4 and $c(k, L\pi)$ and $c(l, L\pi^*)$ we can readily account for $R_\gamma^{kl}(L\pi,L\pi^*)$ in terms of magnitude, sign and dependence on ω. We notice that the $n\alpha^\pi \rightarrow m\beta^\pi$ single ligand transitions contribute to $\langle L\pi|\hat{o}|L\pi^*\rangle$ with nonzero magnetic transition moments along the local x'-axis and with nonzero electric transition moments along the long y'-axis for x, y, and z polarization. Note that the $n\alpha^\pi \rightarrow m\alpha^\pi$ single ligand transition has no magnetic transition dipole contribution. It is also noted that results for transition integrals of the type $\langle L\sigma|\hat{o}|L\sigma^*\rangle$ share the same features as those presented in Table 4 for $\langle L\pi|\hat{o}|L\pi^*\rangle$ and will not be discussed again.

Contributions to R of one-electron excitations $k \rightarrow l$ from $L\sigma \rightarrow L\pi^*$ transitions can be studied in a similar way. Thus, $\langle L\sigma|\hat{o}|L\pi^*$ can be expressed, as shown in Tables 5 and 6, in terms of single ligand transition moments due to L_1 of Scheme 4. We see that the $n\alpha^\sigma \rightarrow m\alpha^\pi$ and $n\beta^\sigma \rightarrow m\beta^\pi$ single ligand transitions have no electric transition dipole contributions.

In some cases the one-electron excitation $k \rightarrow l$ can have contributions from more than one type of transition (d-to-d, $L\sigma \rightarrow L\pi^*$, $L\pi \rightarrow L\pi^*$, or $L\sigma \rightarrow L\sigma^*$) when one or both of the orbitals (k, l) involved are mixtures of different types of obitals (d, $L\sigma$, $L\pi$). In this case the electric transition dipole moment might be due to one type of one-electron excitation and the magnetic transition dipole moment due to another.

Scheme 4. Directions of the Electric and Magnetic Transition Dipole Moments Associated with the Long-Axis $\pi \rightarrow \pi^*$ Excitations in One Ligand

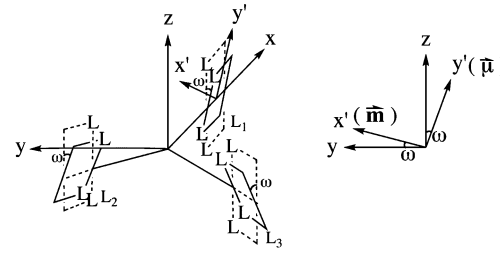

We shall now use the concepts developed here to analyze the calculated CD spectra discussed in section 3.4.

3.4. Comparison of Simulated and Experimental CD Spectra. We compare in Figures 8−11 simulated and experimental CD spectra for the four different systems. The position of the computed excitation energies and the sign and magnitude of each calculated rotatory strength are indicated by bars. Experimental data for Λ-$Co(acac)_3$, Δ-$[Co(Thiox)_3]^{3-}$, and Λ-$[Co(ox)_3]^{3-}$, Δ-$[Co(mal)_3]^{3-}$ were taken from refs 35, 36, and 37, respectively. Unless otherwise stated, both theoretical and experimental spectra refer to the condensed phase with water as the solvent. A global red shift of 4×10^3 cm^{-1} has been applied to all the simulated CD spectra to facilitate the comparison between calculated and experimental data. Intensities for the high-energy part of the experimental CD spectrum of $[Co(ox)_3]^{3-}$ and $[Co(mal)_3]^{3-}$ are magnified by a factor of 20 for the same purpose.

Δ-$[Co(Thiox)_3]^{3-}$. The actual calculated molecular orbital diagrams for all the complexes studied here are displayed in Figure 7 where the orbital splitting and dominant composition (in parentheses) are given with reference to the qualitative diagram in Figure 6. Among the σ-type Thiox MOs in the valence region are the sulfur nonbonding lone-pair orbitals and the bonding σ-orbitals. The contribution from these orbitals to the MOs in $[Co(Thiox)_3]^{3-}$ are denoted as $L\sigma$ and $L\sigma'$ respectively in Figure 7. A similar nomenclature will be used for the other systems studied here.

It follows from the molecular level diagram for $[Co(Thiox)_3]^{3-}$ shown in Figure 7 that the ligand-based orbitals of lowest energy are the σ-type $1a_1^\sigma$ and $1e^\sigma$ combinations. Next to the middle of the diagram are the stabilized ligand-based orbitals of e and a_1 symmetry as well as the nonbonding a_2 levels. The HOMOs, 7e and $4a_1$ of the t_{2g} parentage, stem from the interaction of the metal dπ-orbitals with both the π-ligand combinations and to a small degree the σ-type combinations. The LUMO is a destabilized ligand π-type orbital. At slightly higher energy is the antibonding dσ orbital of e_g parentage.

The simulated and experimental CD spectra are displayed in Figure 8. The relevant computed spectral information is summarized in Table 7 where the major contributions to the transitions are given in terms of dominant one-electron excitations. There is a fairly good agreement between theory and experiment, especially in the high-energy region, with all main features of the experimental spectrum reproduced by the computations. The CD bands in the low energy region ($15-21.9 \times 10^3$ cm^{-1}) have been previously assigned to

Table 4. Transition Integrals of the Type $\langle L\pi|\hat{\mathbf{o}}|L\pi^*\rangle$ in Terms of Single Ligand Transition Moments

$L\pi \cdot L\pi^{*a,b}$	$\hat{\mathbf{o}} = \hat{\boldsymbol{\mu}}^{c,d}$	$\hat{\boldsymbol{o}} = \hat{\boldsymbol{m}}^{c,d}$	CD active direction of polarization
$a_1 \cdot a_1$	0	0	
$a_1 \cdot a_2$	$\cos\ \omega\langle\alpha^\pi\|\mu_{y'}\|\beta^\pi\rangle$	$\sin\ \omega\langle\beta^\pi\|m_{x'}\|\alpha^\pi\rangle$	z
$a_1 \cdot 1e_x$	$\sqrt{1/2}\ \langle\alpha^\pi\|\mu_{z'}\|\alpha^\pi\rangle$	0	
$a_1 \cdot 1e_y$	$\sqrt{1/2}\ \langle\alpha^\pi\|\mu_{z'}\|\alpha^\pi\rangle$	0	
$a_1 \cdot 2e_x$	$\sqrt{1/2}\ \sin\ \omega\langle\alpha^\pi\|\mu_{y'}\|\beta^\pi\rangle$	$-\sqrt{1/2}\ \cos\ \omega\langle\beta^\pi\|m_{x'}\|\alpha^\pi\rangle$	x
$a_1 \cdot 2e_y$	$\sqrt{1/2}\ \sin\ \omega\langle\alpha^\pi\|\mu_{y'}\|\beta^\pi\rangle$	$-\sqrt{1/2}\ \cos\ \omega\langle\beta^\pi\|m_{x'}\|\alpha^\pi\rangle$	y
$a_2 \cdot a_2$	0	0	
$a_2 \cdot 1e_y$	$\sqrt{1/2}\ \sin\ \omega\langle\alpha^\pi\|\mu_{y'}\|\beta^\pi\rangle$	$-\sqrt{1/2}\ \cos\ \omega\langle\beta^\pi\|m_{x'}\|\alpha^\pi\rangle$	x
$a_2 \cdot 1e_x$	$-\sqrt{1/2}\ \sin\ \omega\langle\alpha^\pi\|\mu_{y'}\|\beta^\pi\rangle$	$\sqrt{1/2}\ \cos\ \omega\langle\beta^\pi\|m_{x'}\|\alpha^\pi\rangle$	y
$a_2 \cdot 2e_y$	$-\sqrt{1/2}\ \langle\beta^\pi\|\mu_{z'}\|\beta^\pi\rangle$	0	
$a_2 \cdot 2e_x$	$\sqrt{1/2}\ \langle\beta^\pi\|\mu_{z'}\|\beta^\pi\rangle$	0	
$1e_x \cdot 1e_x$	$1/2\langle\alpha^\pi\|\mu_{z'}\|\alpha^\pi\rangle$	0	
$1e_x \cdot 1e_y$	$-1/2\langle\alpha^\pi\|\mu_{z'}\|\alpha^\pi\rangle$	0	
$1e_y \cdot 1e_y$	$-1/2\langle\alpha^\pi\|\mu_{z'}\|\alpha^\pi\rangle$	0	
$2e_x \cdot 2e_x$	$-1/2\langle\beta^\pi\|\mu_{z'}\|\beta^\pi\rangle$	0	
$2e_x \cdot 2e_y$	$1/2\langle\beta^\pi\|\mu_{z'}\|\beta^\pi\rangle$	0	
$2e_y \cdot 2e_y$	$1/2\langle\beta^\pi\|\mu_{z'}\|\beta^\pi\rangle$	0	
$1e_x \cdot 2e_x$	$-1/2\ \sin\ \omega\langle\alpha^\pi\|\mu_{y'}\|\beta^\pi\rangle$	$1/2\ \cos\ \omega\langle\beta^\pi\|m_{x'}\|\alpha^\pi\rangle$	x
$1e_y \cdot 2e_y$	$1/2\ \sin\ \omega\langle\alpha^\pi\|\mu_{y'}\|\beta^\pi\rangle$	$-1/2\ \cos\ \omega\langle\beta^\pi\|m_{x'}\|\alpha^\pi\rangle$	x
$1e_x \cdot 2e_y$	$1/2\ \sin\ \omega\langle\alpha^\pi\|\mu_{y'}\|\beta^\pi\rangle$	$-1/2\ \cos\ \omega\langle\beta^\pi\|m_{x'}\|\alpha^\pi\rangle$	y
	$-\cos\ \omega\langle\alpha^\pi\|\mu_{y'}\|\beta^\pi\rangle$	$-\sin\ \omega\langle\beta^\pi\|m_{x'}\|\alpha^\pi\rangle$	z
$1e_y \cdot 2e_x$	$1/2\ \sin\ \omega\langle\alpha^\pi\|\mu_{y'}\|\beta^\pi\rangle$	$-1/2\ \cos\ \omega\langle\beta^\pi\|m_{x'}\|\alpha^\pi\rangle$	y
	$\cos\ \omega\langle\alpha^\pi\|\mu_{y'}\|\beta^\pi\rangle$	$\sin\ \omega\langle\beta^\pi\|m_{x'}\|\alpha^\pi\rangle$	z
$\sqrt{1/2}\ (1e_x \cdot 2e_x + 1e_y \cdot 2e_y)$	0	0	
$\sqrt{1/2}\ (1e_x \cdot 2e_y - 1e_y \cdot 2e_x)$	$-\sqrt{2}\ \cos\ \omega\langle\alpha^\pi\|\mu_{y'}\|\beta^\pi\rangle$	$-\sqrt{2}\ \sin\ \omega\langle\beta^\pi\|m_{x'}\|\alpha^\pi\rangle$	z
$\sqrt{1/2}\ (1e_x \cdot 2e_x - 1e_y \cdot 2e_y)$	$-\sqrt{1/2}\ \sin\ \omega\langle\alpha^\pi\|\mu_{y'}\|\beta^\pi\rangle$	$\sqrt{1/2}\ \cos\ \omega\langle\beta^\pi\|m_{x'}\|\alpha^\pi\rangle$	x
$\sqrt{1/2}\ (1e_x \cdot 2e_y + 1e_y \cdot 2e_x)$	$\sqrt{1/2}\ \sin\ \omega\langle\alpha^\pi\|\mu_{y'}\|\beta^\pi\rangle$	$-\sqrt{1/2}\ \cos\ \omega\langle\beta^\pi\|m_{x'}\|\alpha^\pi\rangle$	y

[a] One-electron transition density with D_3 symmetry designation. [b] Refer to Table 1 and Figure 5 for the symmetry ligand orbitals. [c] $\langle i|\hat{\boldsymbol{o}}_v^1|j\rangle = \langle i|\hat{\boldsymbol{o}}_v^2|j\rangle = \langle i|\hat{\boldsymbol{o}}_v^3|j\rangle$, v indicates the x', y', or z' components in the local ligand coordinate system, and the superscript denotes the numbering of ligands. [d] Refer to Table 1 and Figure 4 for single ligand orbitals α^π and β^π.

Table 5. Transition Integrals of Type $\langle L\sigma(\alpha)|\hat{\mathbf{o}}|L\pi^*(\beta)\rangle$ in Terms of Single Ligand Transition Moments

$L\sigma \cdot L\pi^{*a,b}$	$\hat{\mathbf{o}} = \hat{\boldsymbol{\mu}}^{c,d}$	$\hat{\mathbf{o}} = \hat{\boldsymbol{m}}^{c,d}$	CD active direction of polarization
$a_1 \cdot a_1$	0	0	
$a_1 \cdot a_2$	$\sin\ \omega\langle\alpha^\sigma\|\mu_{x'}\|\beta^\pi\rangle$	$\cos\ \omega\langle\beta^\pi\|m_{y'}\|\alpha^\sigma\rangle$	z
$a_1 \cdot 1e_x$	0	$-\sqrt{1/2}\ \langle\alpha^\pi\|m_{z'}\|\alpha^\sigma\rangle$	
$a_1 \cdot 1e_y$	0	$-\sqrt{1/2}\ \langle\alpha^\pi\|m_{z'}\|\alpha^\sigma\rangle$	
$a_1 \cdot 2e_x$	$\sqrt{1/2}\ \cos\ \omega\langle\alpha^\sigma\|\mu_{x'}\|\beta^\pi\rangle$	$-\sqrt{1/2}\ \sin\ \omega\langle\beta^\pi\|m_{y'}\|\alpha^\sigma\rangle$	x
$a_1 \cdot 2e_y$	$\sqrt{1/2}\ \cos\ \omega\langle\alpha^\sigma\|\mu_{x'}\|\beta^\pi\rangle$	$-\sqrt{1/2}\ \sin\ \omega\langle\beta^\pi\|m_{y'}\|\alpha^\sigma\rangle$	y
$1e_x \cdot a_1$	0	$-\sqrt{1/2}\ \langle\alpha^\pi\|m_{z'}\|\alpha^\sigma\rangle$	
$1e_x \cdot a_2$	$-\sqrt{1/2}\ \cos\ \omega\langle\alpha^\sigma\|\mu_{x'}\|\beta^\pi\rangle$	$\sqrt{1/2}\ \sin\ \omega\langle\beta^\pi\|m_{y'}\|\alpha^\sigma\rangle$	y
$1e_x \cdot 1e_x$	0	$1/2\langle\alpha^\pi\|m_{z'}\|\alpha^\sigma\rangle$	
$1e_x \cdot 1e_y$	0	$1/2\langle\alpha^\pi\|m_{z'}\|\alpha^\sigma\rangle$	
$1e_x \cdot 2e_x$	$1/2\ \cos\ \omega\langle\alpha^\sigma\|\mu_{x'}\|\beta^\pi\rangle$	$-1/2\ \sin\ \omega\langle\beta^\pi\|m_{y'}\|\alpha^\sigma\rangle$	x
$1e_x \cdot 2e_y$	$-1/2\ \cos\ \omega\langle\alpha^\sigma\|\mu_{x'}\|\beta^\pi\rangle$	$1/2\ \sin\ \omega\langle\beta^\pi\|m_{y'}\|\alpha^\sigma\rangle$	y
	$-\sin\ \omega\langle\alpha^\sigma\|\mu_{x'}\|\beta^\pi\rangle$	$-\cos\ \omega\langle\beta^\pi\|m_{y'}\|\alpha^\sigma\rangle$	z
$1e_y \cdot a_1$	0	$-\sqrt{1/2}\ \langle\alpha^\pi\|m_{z'}\|\alpha^\sigma\rangle$	
$1e_y \cdot a_2$	$\sqrt{1/2}\ \cos\ \omega\langle\alpha^\sigma\|\mu_{x'}\|\beta^\pi\rangle$	$-\sqrt{1/2}\ \sin\ \omega\langle\beta^\pi\|m_{y'}\|\alpha^\sigma\rangle$	x
$1e_y \cdot 1e_x$	0	$-1/2\langle\alpha^\pi\|m_{z'}\|\alpha^\sigma\rangle$	
$1e_y \cdot 1e_y$	0	$-1/2\langle\alpha^\pi\|m_{z'}\|\alpha^\sigma\rangle$	
$1e_y \cdot 2e_x$	$-1/2\ \cos\ \omega\langle\alpha^\sigma\|\mu_{x'}\|\beta^\pi\rangle$	$1/2\ \sin\ \omega\langle\beta^\pi\|m_{y'}\|\alpha^\sigma\rangle$	y
	$\sin\ \omega\langle\alpha^\sigma\|\mu_{x'}\|\beta^\pi\rangle$	$\cos\ \omega\langle\beta^\pi\|m_{y'}\|\alpha^\sigma\rangle$	z
$1e_y \cdot 2e_y$	$-1/2\ \cos\ \omega\langle\alpha^\sigma\|\mu_{x'}\|\beta^\pi\rangle$	$1/2\ \sin\ \omega\langle\beta^\pi\|m_{y'}\|\alpha^\sigma\rangle$	x
$\sqrt{1/2}\ (1e_x \cdot 2e_x + 1e_y \cdot 2e_y)$	0	0	
$\sqrt{1/2}\ (1e_x \cdot 2e_y - 1e_y \cdot 2e_x)$	$-\sqrt{2}\ \sin\ \omega\langle\alpha^\sigma\|\mu_{x'}\|\beta^\pi\rangle$	$-\sqrt{2}\ \cos\ \omega\langle\beta^\pi\|m_{y'}\|\alpha^\sigma\rangle$	z
$\sqrt{1/2}\ (1e_x \cdot 2e_x - 1e_y \cdot 2e_y)$	$\sqrt{1/2}\ \cos\ \omega\langle\alpha^\sigma\|\mu_{x'}\|\beta^\pi\rangle$	$-\sqrt{1/2}\ \sin\ \omega\langle\beta^\pi\|m_{y'}\|\alpha^\sigma\rangle$	x
$\sqrt{1/2}\ (1e_x \cdot 2e_y + 1e_y \cdot 2e_x)$	$-\sqrt{1/2}\ \cos\ \omega\langle\alpha^\sigma\|\mu_{x'}\|\beta^\pi\rangle$	$\sqrt{1/2}\ \sin\ \omega\langle\beta^\pi\|m_{y'}\|\alpha^\sigma\rangle$	y

[a] One-electron transition density with D_3 symmetry designation. [b] Refer to Table 1 and Figure 5 for the symmetry ligand orbitals. [c] $\langle i|\hat{\boldsymbol{o}}_v^1|j\rangle = \langle i|\hat{\boldsymbol{o}}_v^2|j\rangle = \langle i|\hat{\boldsymbol{o}}_v^3|j\rangle$, v indicates the x', y', or z' components in the local ligand coordinate system, and the superscript denotes the numbering of ligands. [d] Refer to Table 1 and Figure 4 for single ligand orbitals α^σ and β^π.

d-to-d excitations.[36] The small positive peak at 15.8×10^3 cm^{-1} (I of Figure 8) and the negative peak at 18.9×10^3 cm^{-1} (II of Figure 8) were considered respectively $^1A_2$ and ^1E components, originating from the $A_{1g} \rightarrow T_{1g}$ (O_h) transition. In addition, the small feature at 20.9×10^3 cm^{-1} (III of Figure 8) was assigned as the E (T_{2g}) band. According to our calculations, band A corresponds to a d-to-Lπ^* transition (7e→8e) responsible for the feature I observed experimentally. The rotatory strength for this transition is positive, in agreement with experiment. On the other hand, band B

(36) Hidaka, J.; Douglas, B. E. *Inorg. Chem.* **1964**, *3*, 1724–1728.

Table 6. Transition Integrals of Type $\langle L\sigma(\beta)|\hat{o}|L\pi^*(\alpha)\rangle$ in Terms of Single Ligand Transition Moments

$L\sigma \cdot L\pi^{*a,b}$	$\hat{\mathbf{o}} = \hat{\boldsymbol{\mu}}^{c,d}$	$\hat{o} = \hat{\boldsymbol{m}}^{c,d}$	CD active direction of polarization
$a_2 \cdot a_1$	$\sin\omega\langle\beta^\sigma\|\mu_{x'}\|\alpha^\pi\rangle$	$\cos\omega\langle\alpha^\pi\|m_{y'}\|\beta^\sigma\rangle$	z
$a_2 \cdot a_2$	0	0	
$a_2 \cdot 1e_x$	$-\sqrt{1/2}\cos\omega\langle\beta^\sigma\|\mu_{x'}\|\alpha^\pi\rangle$	$\sqrt{1/2}\sin\omega\langle\alpha^\pi\|m_{y'}\|\beta^\sigma\rangle$	y
$a_2 \cdot 1e_y$	$\sqrt{1/2}$ os $\omega\langle\beta^\sigma\|\mu_{x'}\|\alpha^\pi\rangle$	$-\sqrt{1/2}\sin\omega\langle\alpha^\pi\|m_{y'}\|\beta^\sigma\rangle$	x
$a_2 \cdot 2e_x$	0	$-\sqrt{1/2}\langle\beta^\pi\|m_{z'}\|\beta^\sigma\rangle$	
$a_2 \cdot 2e_y$	0	$\sqrt{1/2}\langle\beta^\pi\|m_{z'}\|\beta^\sigma\rangle$	
$2e_x \cdot a_1$	$\sqrt{1/2}\cos\omega\langle\beta^\sigma\|\mu_{x'}\|\alpha^\pi\rangle$	$-\sqrt{1/2}\sin\omega\langle\alpha^\pi\|m_{y'}\|\beta^\sigma\rangle$	x
$2e_x \cdot a_2$	0	$-\sqrt{1/2}\langle\beta^\pi\|m_{z'}\|\beta^\sigma\rangle$	
$2e_x \cdot 1e_x$	$1/2\cos\omega\langle\beta^\sigma\|\mu_{x'}\|\alpha^\pi\rangle$	$-1/2\sin\omega\langle\alpha^\pi\|m_{y'}\|\beta^\sigma\rangle$	x
$2e_x \cdot 1e_y$	$-1/2\cos\omega\langle\beta^\sigma\|\mu_{x'}\|\alpha^\pi\rangle$	$1/2\sin\omega\langle\alpha^\pi\|m_{y'}\|\beta^\sigma\rangle$	y
	$\sin\omega\langle\beta^\sigma\|\mu_{x'}\|\alpha^\pi\rangle$	$\cos\omega\langle\alpha^\pi\|m_{y'}\|\beta^\sigma\rangle$	z
$2e_x \cdot 2e_x$	0	$-1/2\langle\beta^\pi\|m_{z'}\|\beta^\sigma\rangle$	
$2e_x \cdot 2e_y$	0	$1/2\langle\beta^\pi\|m_{z'}\|\beta^\sigma\rangle$	
$2e_x \cdot a_1$	$\sqrt{1/2}\cos\omega\langle\beta^\sigma\|\mu_{x'}\|\alpha^\pi\rangle$	$-\sqrt{1/2}\sin\omega\langle\alpha^\pi\|m_{y'}\|\beta^\sigma\rangle$	y
$2e_x \cdot a_2$	0	$\sqrt{1/2}\langle\beta^\pi\|m_{z'}\|\beta^\sigma\rangle$	
$2e_y \cdot 1e_x$	$-1/2\cos\omega\langle\beta^\sigma\|\mu_{x'}\|\alpha^\pi\rangle$	$1/2\sin\omega\langle\alpha^\pi\|m_{y'}\|\beta^\sigma\rangle$	y
	$-\sin\omega\langle\beta^\sigma\|\mu_{x'}\|\alpha^\pi\rangle$	$-\cos\omega\langle\alpha^\pi\|m_{y'}\|\beta^\sigma\rangle$	z
$2e_y \cdot 1e_y$	$-1/2\cos\omega\langle\beta^\sigma\|\mu_{x'}\|\alpha^\pi\rangle$	$1/2\sin\omega\langle\alpha^\pi\|m_{y'}\|\beta^\sigma\rangle$	x
$2e_y \cdot 2e_x$	0	$1/2\langle\beta^\pi\|m_{z'}\|\beta^\sigma\rangle$	
$2e_y \cdot 2e_y$	0	$1/2\langle\beta^\pi\|m_{z'}\|\beta^\sigma\rangle$	
$\sqrt{1/2}(2e_x \cdot 1e_x + 2e_y \cdot 1e_y)$	0	0	
$\sqrt{1/2}(2e_x \cdot 1e_y - 2e_y \cdot 1e_x)$	$\sqrt{2}\sin\omega\langle\beta^\sigma\|\mu_{x'}\|\alpha^\pi\rangle$	$\sqrt{2}\cos\omega\langle\alpha^\pi\|m_{y'}\|\beta^\sigma\rangle$	z
$\sqrt{1/2}(2e_x \cdot 1e_x - 2e_y \cdot 1e_y)$	$\sqrt{1/2}\cos\omega\langle\beta^\sigma\|\mu_{x'}\|\alpha^\pi\rangle$	$-\sqrt{1/2}\sin\omega\langle\alpha^\pi\|m_{y'}\|\beta^\sigma\rangle$	x
$\sqrt{1/2}(2e_x \cdot 1e_y + 2e_y \cdot 1e_x)$	$-\sqrt{1/2}\cos\omega\langle\beta^\sigma\|\mu_{x'}\|\alpha^\pi\rangle$	$\sqrt{1/2}\sin\omega\langle\alpha^\pi\|m_{y'}\|\beta^\sigma\rangle$	y

[a] One-electron transition density with D_3 symmetry designation. [b] Refer to Table 1 and Figure 5 for the symmetry ligand orbitals. [c] $\langle i|\hat{o}_v^1|j\rangle = \langle i|\hat{o}_v^2|j\rangle = \langle i|\hat{o}_v^3|j\rangle$, v indicates the x', y', or z' components in the local ligand coordinate system, and the superscript denotes the numbering of ligands. [d] Refer to Table 1 and Figure 4 for single ligand orbitals β^σ and α^π.

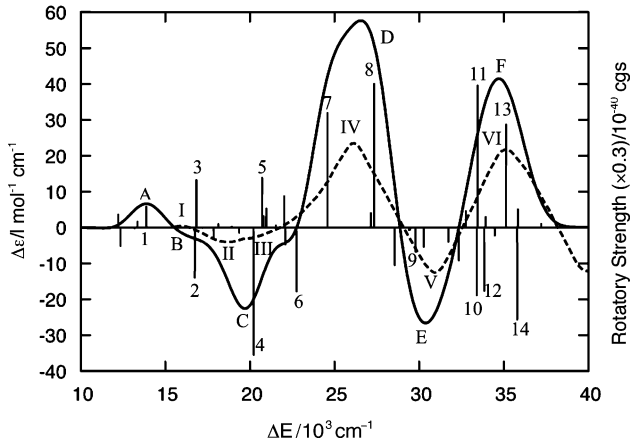

Figure 8. Simulated (solid) and experimental (dashed) CD spectra for Δ-$[Co(Thiox)_3]^{3-}$. Calculated excitation energies and rotatory strengths are indicated by bars. Computed rotatory strengths were scaled by a factor of 0.3. The calculated excitations are red-shifted by 4×10^3 cm^{-1}. Bands in the experimental spectrum are indicated by Roman numerals. Bands in the simulated spectrum are indicated by alphabetic letters.

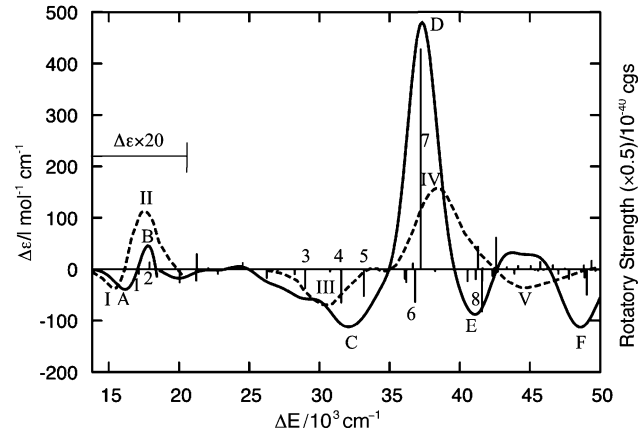

Figure 9. Simulated (solid) and experimental (dashed) CD spectra for Λ-$Co(acac)_3$. Ethanol was used as solvent. Calculated excitation energies and rotatory strengths are indicated by bars. Computed rotatory strengths were scaled by a factor of 0.5. The calculated excitations are red-shifted by 4×10^3 cm^{-1}. The low-energy part of both the simulated and experimental spectra is magnified by a factor of 20. Bands in the experimental spectrum are indicated by Roman numerals. Bands in the simulated spectrum are indicated by alphabetic letters.

contains both the E (2) and A_2 (3) components of the $A|_g \rightarrow T|_g$ (O_h) d-to-d transitions and is assigned to region II of the experimental spectrum. The two components are too close to be resolved and appear as one band. The sign pattern for the E and A_2 components of the $A|_g \rightarrow T|_g$ transition in Δ-$[Co(Thiox)_3]^{3-}$ is the same as for Δ-$[Co(en)_3]^{3+}$. The T_{2g} band predicted by theory is in the same energy region as E (2) and A_2 (3) but its R-value is too small to be seen on the bar spectrum. The band C, which seems to overlap with the B-band, is ascribed to the $\pi \rightarrow \pi^*$ transitions (4). We assign region III of the experimental spectrum to these transitions.

The features of the theoretical and the experimental CD spectra agree especially well with each other in the higher energy region. The three intense CD bands (IV, V, and VI) of the observed spectrum in this region ($22-40 \times 10^3$ cm^{-1}) have been related to internal ligand transitions.[36] Our TD-DFT results of bands D, E, and F indicate, however, that the situation is not quite so clear-cut as there are also contributions from L_πMCT (6), L_σMCT (8 and 9), and ML_πCT (13). A common feature in tris(bidentate) complexes is the $A|_g \rightarrow T|_u$ (O_h) L_σMCT transitions. They are in the present system identified as excitations 8 (E component) and 9 (A_2 component)), respectively.

It can been seen from Figure 8 and Table 7 that there are a large number of transitions with different characters involved in the CD spectrum of $[Co(Thiox)_3]^{3-}$, which makes the overall features of the spectrum somewhat more com-

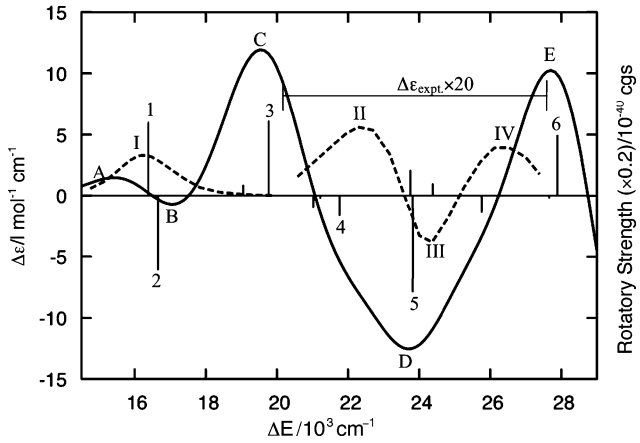

Figure 10. Simulated (solid) and experimental (dashed) CD spectra for Λ-$[Co(ox)_3]^{3-}$. Calculated excitation energies and rotatory strengths are indicated by bars. Computed rotatory strengths were scaled by a factor of 0.2. The calculated excitations are red-shifted by 4×10^3 cm^{-1}. The higher energy part of the experimental CD spectrum is magnified by a factor of 20. Bands in the experimental spectrum are indicated by Roman numerals. Bands in the simulated spectrum are indicated by alphabetic letters.

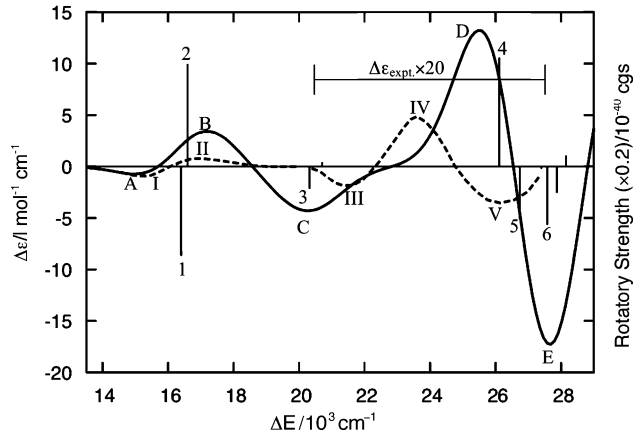

Figure 11. Simulated (solid) and experimental (dashed) CD spectra for Δ-$[Co(mal)_3]^{3-}$. Calculated excitation energies and rotatory strengths are indicated by bars. Computed rotatory strengths were scaled by a factor of 0.2. The calculated excitations are red-shifted by 4×10^3 cm^{-1}. The higher energy part of the experimental CD spectrum is magnified by a factor of 20. Bands in the experimental spectrum are indicated by Roman numerals. Bands in the simulated spectrum are indicated by alphabetic letters.

plicated in comparison to those of the diamine complexes where only σ-orbitals are involved. We shall now make use of the discussion in section 3.3 to analyze the mechanism by which these transitions contribute to the CD of the complexes.

For band A (E symmetry) that is ascribed to a $ML_\pi CT$ mainly caused by the 7e→8e one-electron excitation (1 in Figure 8), the analysis reveals that the rotatory strength is primarily due to contributions of the type $\langle L\pi|\hat{o}|L\pi^*\rangle$ associated with ligand $\pi\rightarrow\pi^*$ transitions. In terms of the specific transition integrals, it has contributions to the electric transition moment from $\langle\beta^\pi|\mu_{z'}|\beta^\pi\rangle$ (Table 4) whereas the magnetic component comes from $\langle\beta^\pi|m_{x'}|\alpha^\pi\rangle$ (Table 4). On the other hand, the transition 13 (7e→$5a_1$) also ascribed to the $ML_\pi CT$ has again a dominant contribution from $\langle L\pi|\hat{o}|L\pi^*\rangle$, but the ligand-centered transitions involved in this case contribute to the rotatory strength as $\langle\alpha^\pi|\mu_{z'}|\alpha^\pi\rangle$ and $\langle\beta^\pi|m_{x'}|\alpha^\pi\rangle$, respectively.

Table 7. Calculated and Experimental Spectral Properties for Δ-$[Co(Thiox)_3]^{3-}$

				one-electron excitation[d]	
no.	R^a (10^{-40} cgs)	ΔE^b (10^3 cm^{-1})	symmetry[c]	MO→MO	%
1	+19.75	17.87	E	7e → 8e	85
2	−47.46	20.74 (18.9)	E	7e → 9e	50
				$4a_1$ → 9e	48
3	+44.78	20.84 (15.8)	A_2	7e → 9e	98
4	−118.99	24.21	E	$3a_2$ → 8e	40
				5e → 8e	18
5	+46.72	24.72	E	6e → 9e	32
				5e → $4a_2$	16
				$3a_1$ → 8e	15
6	−60.24	26.74	E	$3a_2$ → 9e	41
				5e → 9e	24
7	+107.03	28.59 (26.1)	E	$2a_2$ → 8e	85
8	+134.13	31.33	E	$2a_2$ → 9e	68
				4e → 8e	14
9	−23.42	33.79	A_2	4e → 9e	54
				$2a_1$ → $4a_2$	40
10	−63.89	37.41	E	1e → $4a_2$	46
				4e → 9e	14
11	+132.65	37.46 (35.5)	E	1e → $4a_2$	48
				2e → 8e	20
12	−59.76	37.84	A_2	1e → 8e	43
				3e → 9e	35
13	+96.37	39.13	E	7e → $5a_1$	83
14	−86.33	39.78	E	3e → 9e	26
				2e → 8e	17

[a] Rotatory strength. [b] Excitation energy; data in parenthesis are experimental values taken from ref 36. [c] Symmetry of the excited state. [d] Major contributions from one-electron excitations to the transition.

Excitation 4 has a predominant $\pi\rightarrow\pi^*$ character that has the major contribution from the one-electron excitations $3a_2$→8e and 5e→8e. The mechanism for generation of optical activity here is quite straightforward and involves the same ligand-centered excitations as discussed above for excitation 1.

Another important excitation we need address is the $L_\pi MCT$ (6) due to electron promotion from orbitals $3a_2$ and 5e to 9e. Since the metal-based d-orbital 9e has a large contribution from ligand σ-orbitals, it is understandable that the associated rotatory strength comes largely from the transition integrals of the type $\langle\beta^\sigma|\mu_{z'}|\beta^\sigma\rangle$ and $\langle\beta^\pi|m_{z'}|\beta^\sigma\rangle$.

We finally have several ligand-localized $\sigma\rightarrow\pi^*$ transitions, that is, 7, 10, 11, and 12 as displayed in Figure 8. TD-DFT analysis indicates that excitations 7, 10, and 11 may acquire their electric transition dipole moment in all cases from $\langle\beta^\pi|\mu_{z'}|\beta^\pi\rangle$ and their magnetic moment from $\langle\beta^\pi|m_{z'}|\beta^\sigma\rangle$. For transition 12, the noticeable d-components in both the occupied (1e) and the virtual (8e) orbitals give rise to a predominant contribution to the magnetic transition moment through $\langle d\sigma|\hat{\boldsymbol{m}}|d\pi\rangle$ whereas the ligand σ-components in the two MOs combine to generate the electric moment through $\langle\alpha^\sigma|\mu_{z'}|\beta^\sigma\rangle$.

Λ-Co(acac)$_3$. Similar to $[Co(Thiox)_3]^{3-}$, the lower energy part of the MO diagram is occupied by the stabilized σ- and π-type ligand-based orbitals, Figure 7. The HOMOs are invariably the metal t_{2g} set. However, unlike the Thiox complex, the metal e_g orbitals now become the LUMOs, followed at higher energy by the destabilized ligand π^*-combinations. Figure 9 compares the simulated and experimental CD spectrum of Λ-$Co(acac)_3$. The agreement is remarkably good. As can be expected from the orbital level

Table 8. Calculated and Experimental Spectral Properties for Λ-Co(acac)$_3$

				one-electron excitation[d]	
no.	R^a (10^{-40} cgs)	ΔE [b] (10^3 cm^{-1})	symmetry[c]	MO→MO	%
1	−20.56	21.14 (15.5)	A_2	4e → 5e	99
2	+28.68	21.89 (17.5)	E	4e → 5e	89
				2a$_1$ → 5e	7
3	−76.58	32.99	E	1a$_2$ → 5e	37
				3e → 6e	27
				3e → 3a$_1$	14
4	−132.92	35.54	A_2	2e → 5e	52
				3e → 6e	35
5	−108.44	37.16	E	2e → 5e	26
				3e → 6e	22
				3e → 3a$_1$	12
6	−130.81	40.81	A_2	1e → 5e	62
				2e → 6e	16
7	+858.20	41.21 (38.2)	E	2e → 5e	49
				1a$_2$ → 5e	14
8	−166.66	45.59(44.4)	A_2	1e → 5e	22
				2e → 5e	17
				3e → 6e	12

[a] Rotatory strength. [b] Excitation energy; data in parenthesis are experimental values taken from ref 35. [c] Symmetry of the excited state. [d] Major contributions from one-electron excitations to the transition.

diagram, the lowest energy region of the CD spectrum reveals two d-to-d bands typical for the σ-bonded tris(bidentate) transition metal complexes. The bands A/I and B/II are assigned, by both theory and experiment, to the A_2 and E components, respectively. The CD bands in the higher energy region of the experimental spectrum were previously assigned to LMCT (III) and ligand $\pi\rightarrow\pi^*$ transitions (IV and V). In partial agreement with the experiment, the region 20 to 40 $\times$ 10^3 cm^{-1} is dominated by CT transitions (C/III, D), that is, from the ligand-based σ-orbitals of t_{1u} parentage (1a$_2$ and 2e, Figure 7) to the LUMO metal e_g set (5e, Figure 7), and the range above 40 $\times$ 10^3 cm^{-1} by ligand $\pi\rightarrow\pi^*$ excitations (E/V). In addition, however, our analysis indicates that the CT and ligand $\pi\rightarrow\pi^*$ excitations cannot be cleanly separated. There are, for example, pronounced character of LMCT (1e→5e) in excitation 8 and of $\pi\rightarrow\pi^*$ in 3−5.

As to the mechanism of associated optical activity, we shall consider the excitations 3−5 and 8, which all have a notable mix of L_σMCT and $\pi\rightarrow\pi^*$ character, see Table 8. It is found that in all cases the ligand-localized $\pi\rightarrow\pi^*$ excitations play a significant role in obtaining the rotatory strengths through $\langle\beta^\pi|\hat{\boldsymbol{o}}|\alpha^\pi\rangle$ for both electric and magnetic transition dipole moments. In addition, ligand σ-orbitals and metal d-orbitals also participate as they usually do in a typical L_σMCT via $\langle L\sigma|\hat{\boldsymbol{\mu}}|L\sigma^*\rangle$ and $\langle d\sigma|\hat{\boldsymbol{m}}|d\pi\rangle$.[34]

Λ-[Co(ox)$_3$]$^{3-}$ and Δ-[Co(mal)$_3$]$^{3-}$. The computed molecular orbital energy levels for [Co(ox)$_3$]$^{3-}$ and [Co(mal)$_3$]$^{3-}$ are also displayed in Figure 7. As we can see, the main features of the two diagrams are quite similar, except that in the latter, the ligand-based π^*-orbitals are well above the empty e_g set of dσ orbitals (7e).

In contrast to other Cr(O−O)$_3$ and Co(O−O)$_3$ complexes, [Co(ox)$_3$]$^{3-}$ was reported[37] to have only one CD band (I) in the d-to-d T_{1g} (O_h) absorption region (14−19 $\times$ 10^3 cm^{-1}), Figure 10. Compared to experiment, our calculations generate in this region two CD bands, that is, A and B, slightly separated with the positive one assigned to E symmetry and the negative to the A_2. The low intensity and asymmetry of the bands are due to extensive cancellation of contributions from the two components (1 and 2 of Table 9) to the bands. The reported CD spectrum reveals also three weak bands (II, III, and IV) in the higher energy region, where a single T_{2g} (O_h) band was expected. The appearance and low rotatory strength of the three bands seems puzzling. They were suggested to be the results of either a chelate ring opening[38,39] or a solvent interaction that lowers the effective symmetry from D_3.[37] The present TD-DFT computations reveal three bands (C, D, and E) with the same sign pattern as II, III, and IV but of much higher intensity in comparison with experiment. While bands C/II and E/IV are ascribed to ML_πCT (3) and L_σMCT (6), respectively, the band D/III has both characters (4 and 5). On the other hand, the calculated d-to-d T_{2g} band, at about 23 $\times$ 10^3 cm^{-1}, is very weak and has nearly no contribution to the spectrum.

As for [Co(mal)$_3$]$^{3-}$, three peaks (III, IV, and V) were also observed in the higher energy region, Figure 11. The simulated spectrum, as shown in Figure 11, exhibits in the same region comparable features (C/III, D/IV, and E/V) that can be attributed to LMCT that involves the ligand-based σ MOs 3a$_2$ (in 3) and 4e (in 4 and 5), and the ligand π-type orbitals 3e (in 6), see Figure 7 and Table 10. In the lower energy region, both theory and experiment exhibit two typical d-to-d bands (A/I and B/II, Figure 11). Early studies[32,37] indicated a possible reversal in the order and signs of the E and A_2 components for the complex [Co(mal)$_3$]$^{3-}$ with the negative component assigned to A_2. However, our calculations do not support such a reversal, with transitions 1 and 2 having E and A_2 symmetry, respectively. The stability of the malonate complex is highly dependent on its environment.[32,40] It might decompose in solution after a few hours at room temperature.[37] The way in which decomposition influences the CD spectrum of the complex might be worth a later study.

We also notice that there are major ligand-to-d excitations, that is, 5 of [Co(ox)$_3$]$^{3-}$ in Figures 10 and 3 of [Co(mal)$_3$]$^{3-}$ in Figure 11, involving the bonding single ligand σ-orbitals. This type of orbital, however, is only of minor importance in the spectra of Thiox and acac systems.

Of interest for the mechanism consideration are the two ML_πCT transitions in [Co(ox)$_3$]$^{3-}$ (3 and 4) as well as the L_πMCT in [Co(mal)$_3$]$^{3-}$ (6). Detailed analysis suggests, for both ML_πCT transitions, a major contribution to the electric transition moment from $\langle\beta^\pi|\mu_z|\beta^\pi\rangle$. The magnetic component of the transitions, however, come from $\langle\beta^\pi|m_x|\alpha^\pi\rangle$ for 3 and $\langle d\sigma|\hat{\boldsymbol{m}}|d\pi\rangle$ for 4, because of the presence of a d-component in orbital 8e involved in transition 4 whereas no symmetry-matched d-orbitals can be mixed into 4a$_2$ responsible for

(37) Russell, R. L. C.; Douglas, B. E. *Inorg. Nucl. Chem. Lett.* **1973**, *9*, 1251–1254.
(38) Mccaffery, A. J.; Mason, S. F.; Ballard, R. E. *J. Chem. Soc.* **1965**, 2883–2892.
(39) Mccaffery, A. J.; Mason, S. F. *Proc. Chem. Soc.* **1962**, 388–389.
(40) Butler, K. R.; Snow, M. R. *J. Chem. Soc., Dalton Trans.* **1976**, 259–262.

Table 9. Calculated Spectral Properties for Λ-$[Co(ox)_3]^{3-}$

				one-electron excitation[d]	
no.	R^a (10^{-40} cgs)	ΔE^b (10^3 cm^{-1})	symmetry[c]	MO→MO	%
1	+30.20	20.39 (16.21)	E	$4a_1 \rightarrow 7e$	53
				$6e \rightarrow 7e$	47
2	−30.57	20.66	A_2	$6e \rightarrow 7e$	99
3	+30.69	23.77	E	$6e \rightarrow 4a_2$	84
4	−8.38	25.76	E	$6e \rightarrow 8e$	92
5	−39.42	27.82	A_2	$5e \rightarrow 7e$	98
6	+24.86	31.89	A_2	$4e \rightarrow 7e$	96

[a] Rotatory strength. [b] Excitation energy; data in parenthesis are experimental values taken from ref 38. [c] Symmetry of the excited state. [d] Major contributions from one-electron excitations to the transition.

Table 10. Calculated Spectral Properties for Δ-$[Co(mal)_3]^{3-}$

				one-electron excitation[d]	
no.	R^a (10^{-40} cgs)	ΔE^b (10^3 cm^{-1})	symmetry[c]	MO→MO	%
1	−43.44	20.40	E	$3a_1 \rightarrow 7e$	54
				$6e \rightarrow 7e$	46
2	+49.85	20.60	A_2	$6e \rightarrow 7e$	100
3	−10.94	24.32	E	$3a_2 \rightarrow 7e$	53
				$6e \rightarrow 7e$	18
4	+52.98	30.11	E	$4e \rightarrow 7e$	87
5	−25.59	30.74	A_2	$4e \rightarrow 7e$	67
				$3e \rightarrow 7e$	27
6	−28.40	31.58	A_2	$3e \rightarrow 7e$	72
				$4e \rightarrow 7e$	24

[a] Rotatory strength. [b] Excitation energy. [c] Symmetry of the excited state. [d] Major contributions from one electron excitations to the transition.

transition 3. The L_πMCT in $[Co(mal)_3]^{3-}$, on the other hand, has a similar origin for the rotatory strength to the L_πMCT in the Thiox complex.

4. Conclusion

In this paper we have presented TD-DFT calculations on the CD spectra of Λ-$Co(acac)_3$, Δ-$[Co(Thiox)_3]^{3-}$, Λ-$[Co(ox)_3]^{3-}$, and Δ-$[Co(mal)_3]^{3-}$. The simulated spectra are compared in great details with experiment. Fairly reasonable agreement is obtained between theory and experiment.

The studied complexes containing unsaturated ligands exhibit more complicated electronic structures and in turn more features of their CD spectra in comparison with the systems of only saturated ligands. In addition to the typical d-to-d transitions and L_σMCT occurring for complexes of saturated ligands, there are also L_πMCT (or ML_πCT) and ligand-centered transitions in the complexes of unsaturated ligands.

Special attention has been given to the mechanism by which transitions that are characteristic for the complexes of unsaturated ligands acquire optical activity. Metal−ligand orbital interactions are rationalized in terms of symmetry unique overlaps between metal d-orbitals and symmetry ligand-combinations. The contribution to the rotatory strengths associated with various transitions is interpreted in terms of transition moments mainly of the type $\langle L\pi|\hat{\mathbf{o}}|L\pi^*\rangle$, $\langle L\sigma|\hat{\mathbf{o}}|L\pi^*\rangle$, or $\langle L\sigma|\hat{\mathbf{o}}|L\sigma^*\rangle$. Although there might be cases where an electronic transition is caused by many one-electron excitations and each one-electron excitation further has contributions from more than one type of transition moments, the origin of the CD can always be easily addressed within the qualitative framework developed here.

Acknowledgment. This work has received financial support from the National Science and Engineering Research Council of Canada (NSERC). One of us (J.F.) would like to acknowledge the financial support of Alberta Ingenuity Fund (AIF). T.Z. would like to thank the Canadian Government for a Canada Research Chair.

IC800072K